



# Firn changes at Colle Gnifetti revealed with a high-resolution process-based physical model approach

Enrico Mattea<sup>1</sup>, Horst Machguth<sup>1</sup>, Marlene Kronenberg<sup>1</sup>, Ward van Pelt<sup>2</sup>, Manuela Bassi<sup>3</sup>, and Martin Hoelzle<sup>1</sup>

<sup>1</sup>Department of Geosciences, University of Fribourg, Fribourg, Switzerland

<sup>2</sup>Department of Earth Sciences, Uppsala University, Uppsala, Sweden

<sup>3</sup>Department of Forecasting Systems, Regional Agency for Environmental Protection of Piedmont, Turin, Italy

**Correspondence:** Enrico Mattea (enrico.mattea@unifr.ch)

**Abstract.** Our changing climate is expected to affect ice core records as cold firn progressively transitions to a temperate state. Thus there is a need to improve understanding and further develop quantitative process modeling, to better predict cold firn evolution under a range of climate scenarios. Here we present the application of a distributed, fully coupled energy balance model, to simulate high-alpine cold firn at Colle Gnifetti over the period 2003–2018. For the first time, we force such a model with high-resolution, long-term and extensively quality-checked meteorological data measured in closest vicinity of the firn site, at the Capanna Margherita (4560 m a.s.l.). The model incorporates the spatial variability of snow accumulation rates, and is calibrated using several, partly unpublished high-altitude measurements from the Monte Rosa area. The simulation reveals a very good overall agreement in the comparison with a large archive of firn temperature profiles. The rate of firn warming at 20 m depth is estimated at 0.44 °C per decade. Our results show that surface melt over the glaciated saddle is increasing by 3–4 mm w.e. yr<sup>-2</sup> depending on the location (29–36 % in 16 years), although with large inter-annual variability. Analysis of modeled melt indicates a marked tendency towards small melt events (< 4 mm w.e.), which collectively represent a significant fraction of the melt totals. Atmospheric humidity is found to be a prominent control over melt occurrence, with considerable amounts of sublimation happening in dry conditions. For future developments, we recommend implementing a physical simulation of meltwater infiltration, to be calibrated with more measurements of percolation in cold firn.

## 1 Introduction

Cold firn and ice – defined by negative temperatures year-round – are recognized as a valuable archive of past atmospheric conditions, accessed through ice cores (Wagenbach et al., 2012). In the recrystallization and recrystallization-infiltration firn facies, meltwater infiltration is respectively absent or limited to the near-surface layer of the firn (Shumskii, 1964; Hoelzle et al., 2011). This enables preservation of the original layering of accumulated snow, which can be dated to provide an atmospheric record including greenhouse gases, aerosols, and isotopic temperature proxies (Wagenbach et al., 2012).

The longest records are found in ice cores from the polar regions. Nonetheless, cold firn is also present in the Alps above 3400–4150 m a.s.l., depending on location and aspect (Suter et al., 2001). Such alpine cold firn is located close to major, historical sources of European anthropogenic emissions, thus providing a particularly valuable record of man-made changes



to atmospheric composition (Wagenbach et al., 2012). Moreover, the Alpine region features a historically high density of meteorological observations as well as other paleoclimatic records (such as tree rings and speleothems), enabling calibration and comparison of the atmospheric archives (Wagenbach et al., 2012).

Beside its importance for ice core studies, cold firn also acts as a buffer against mass losses brought upon glaciers by a warming climate. Specifically, meltwater refreezing close to the surface does not contribute to water runoff: thus an increased input in the firn surface energy balance (SEB), with enhanced meltwater production, does not directly affect mass balance (e.g., Harper et al., 2012). As a result, rising temperatures – instead of mass losses – are the main expression of 20th-century atmospheric warming in cold firn (Haeberli and Beniston, 1998; Buri, 2013).

Climate change is expected to trigger a progressive transition from cold to temperate firn, naturally advancing from the lower elevations towards the higher (Darms, 2009). Expected consequences for sites of presently cold firn are the onset of mass loss and an irremediable degradation of the climatic archive, induced by meltwater infiltration to increasing depths (Hoelzle et al., 2011; de Blasi et al., 2019). Then a better understanding of this transition will become crucial to the continued viability of ice core campaigns, as well as the prediction of future runoff regimes in high-alpine and polar catchments. Particularly valuable will be the acquisition of quantitative modeling capabilities and localized information on timing and uncertainties of firn changes, also incorporating the regularly updated climatic scenarios.

Among alpine cold firn sites, the Colle Gnifetti saddle (CG; Fig. 1) in the Monte Rosa range (4450 m a.s.l., Swiss/Italian Alps) stands out for the dense coverage of glaciological measurements, acquired continuously over almost 50 years. The very low annual accumulation rates of the area (between 0.3 and 1.2 m w.e.) enable ice core records covering the last millennium and potentially extending into the late Pleistocene, more than any other glaciated site in the Alps (Jenk et al., 2009; Wagenbach et al., 2012; Bohleber et al., 2018). Important climatological results from CG ice cores include a 1200-year time series of air temperature, reconstructed from mineral dust proxies (Bohleber et al., 2018), as well as a glacio-chemical record of anthropogenic alterations to atmospheric composition, starting before industrialization and extending to the recent emission reductions of some pollutant species (Schwikowski, 2004; Barbante et al., 2004; More et al., 2017; Gabrieli et al., 2011).

Parallel to ice core investigations, borehole measurements starting in 1976 (Haeberli and Funk, 1991) provide a detailed picture of the thermal conditions at the CG saddle. Firn temperatures below the depth of annual fluctuations (about 18 m) range from -13.5 °C to -10 °C, depending on aspect (Suter and Hoelzle, 2002). Haeberli and Funk (1991) found almost steady-state temperature conditions in englacial profiles from 1983, noting only a weak influence of meltwater refreezing. Lüthi and Funk (2001) reported temperature profiles from 1995 having striking bends at a depth of about 30 m, and interpreted them as the first published clues to a non-steady firn warming situation. Subsequently, Hoelzle et al. (2011) found evidence of accelerated englacial warming exceeding the air temperature increase, exposing an enhanced role of meltwater percolation.

Several studies have previously applied simple firn models at CG, to reproduce englacial temperatures from idealized boundary conditions (Haeberli and Funk, 1991; Lüthi, 2000; Lüthi and Funk, 2001). Suter (2002) presented a distributed model study of the area, simulating one year of SEB at daily resolution, and formulated one-dimensional firn temperature predictions according to a simple parametric model. Buri (2013) used the coupled model GeoTOP to simulate energy balance and sub-surface temperatures at several locations in the CG area.

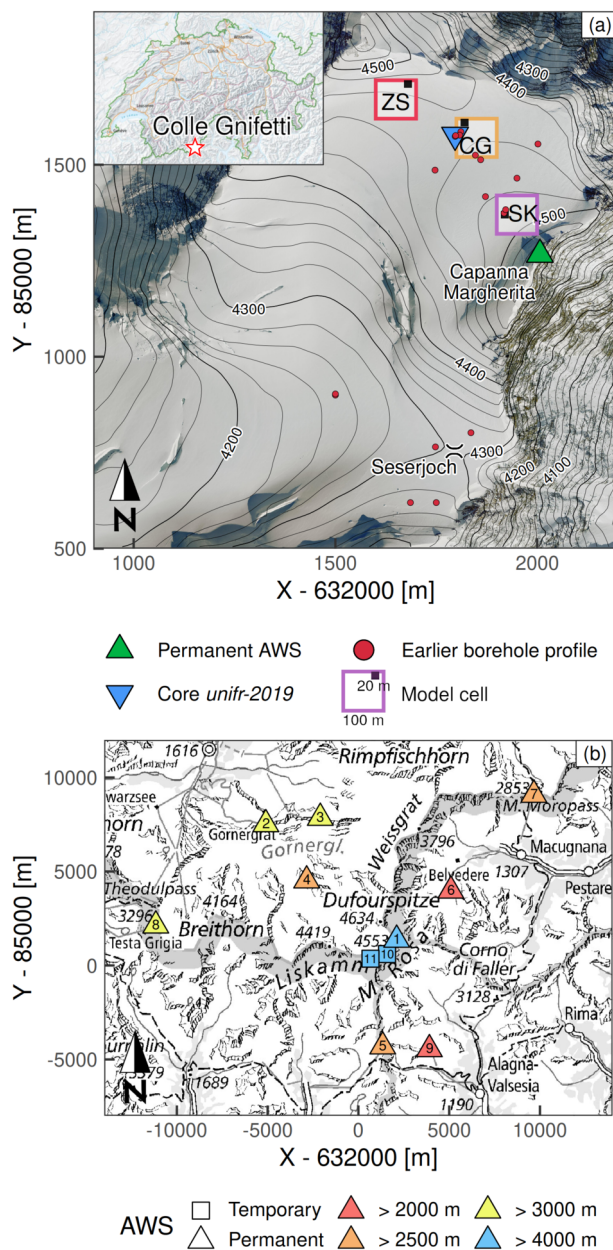


**Figure 1.** (a) Colle Gnifetti location map. Labeled model cells correspond to the point series in Fig. 6–9. ZS: Zumsteinspitze slope; CG: Colle Gnifetti saddle point; SK: Signalkuppe slope. Several borehole locations were measured more than once (also see Fig. 5). (b) Overview map of the Monte Rosa range with AWS locations (see Table 2 for more information). In both panels X and Y are metric CH1903/LV03 coordinates. Orthophoto and topographic map source: Federal Office of Topography swisstopo.



A major challenge for firn models at CG is the complex boundary condition of surface accumulation: the low accumulation  
60 rates are due to an extreme wind scouring of the snow surface, favored by the west-east saddle orientation. This process  
is countered by solar radiation through melt consolidation. Thus snow accumulation has a strong spatial gradient according  
to terrain aspect and is biased towards summer; a significant interannual variability is also observed (Alean et al., 1983;  
Wagenbach et al., 2012). Surface accumulation directly controls the cold content and initial stratigraphy of the firn. However,  
the complex accumulation patterns at CG have not been addressed in past modeling studies, even within models coupling the  
65 energy balance to the sub-surface. Suter et al. (2001) considered accumulation only as a proxy for vertical velocities at the  
surface, to account for ice advection in a minimal firn temperature model. Buri (2013) only simulated individual borehole  
locations in the CG area, relying for all of them on weather data collected at the Corvatsch automatic weather station (AWS),  
almost 160 km away and over 1 km lower in altitude. More recently, Licciulli (2018) established a flow model independent on  
surface accumulation, and obtained distributed accumulation from the model on the assumption of steady state conditions.

70 Moreover, surface melt – increasingly occurring at high altitudes in a warming climate – is expected to play a central role  
in the transition from cold to temperate firn. Gilbert et al. (2014) found on Mont Blanc that melt patterns can strongly affect  
the overall energy balance of a cold firn pack in summer. To this day, little knowledge exists on the atmospheric conditions  
leading to melt events in cold firn, or the dynamics of such melt events. Suter et al. (2001) modeled CG firn temperatures with  
a 1 day time-step, too coarse compared to the time scales of melt and infiltration processes. Buri (2013), while using an hourly  
75 time-step, did not examine melt amounts and dynamics. Licciulli (2018), focusing on ice flow, modeled the firn at CG with a 1  
year time-step, assuming no meltwater infiltration in the firn.

Here, we present the application of a physically-based coupled model to simulate firn evolution at CG, over a 16 year period  
on a high-resolution gridded domain. After validation against a large archive of firn temperature measurements, the model is  
used to investigate the conditions and dynamics of high-alpine melt events. For the first time, model forcing is based on the  
80 extensively processed hourly time series of the Capanna Margherita (CM) AWS (Martorina et al., 2003), which benefits from  
an exceptional location at 4560 m a.s.l. and within 400 m of the CG saddle point.

The data used within the study are described in Sect. 2, the coupled model in Sect. 3, the results are presented in Sect. 4 and  
discussed in Sect. 5, while the last section provides the conclusions and some perspectives for future cold firn research.

## 2 Data

### 85 2.1 Meteorological time series

Meteorological forcing of the coupled model consists of an hourly time series, describing air temperature, atmospheric pressure,  
wind speed, relative humidity, fractional cloud cover and precipitation (Fig. 2). The series was primarily assembled using  
data from the CM AWS, located on the Signalkuppe summit at 4560 m a.s.l. (Fig. 1a). The station records air temperature,  
barometric pressure, wind speed and direction, and global radiation (Table 1). The measured parameters are available as hourly  
90 instantaneous values.



**Table 1.** Sensors installed at the CM AWS.

Parameter	Sensor	Notes
Air temperature	CAE TU20 thermometer	Rated accuracy 0.2 °C Rated ambient radiation influence < 0.8 °C Not artificially ventilated
Barometric pressure	CAE BA20 barometer	Rated accuracy 0.5 hPa
Global radiation	CAE HE20/K pyranometer	Rated daily accuracy 5 % Wavelength band 305–2800 nm
Wind speed	CAE VV20 cup taco-anemometer	Rated accuracy 0.07 m s <sup>-1</sup> or 1 %
Wind direction	CAE DV20 gonio-anemometer	Rated accuracy 2.8°

The consistent availability (> 95 %) of long-term data (since mid-2002) makes the series a valuable data-set for high-alpine research. Still, an extensive evaluation and processing of the data is essential due to the extreme measuring conditions (Martorina et al., 2003). In particular, freezing of the anemometer – as well as snow and ice accumulation interfering with the pyranometer – are relatively common occurrences. Therefore, the hourly data from eight other high-altitude AWS located in the region (Fig. 1b, id 2–9 in Table 2) were used to perform quality checks, to fill gaps in the CM time series, and to provide data for parameters not measured at CM. The selection of stations to include was determined by the availability of different parameters measured at each site, by the effort to provide an unbiased geographic coverage in all directions from the CM AWS, and by the station tendency towards concurrent failures in challenging conditions, such as winter storms.

All AWS series were pre-processed to remove clock errors, detected with cross-correlation analysis. Then each series was entirely reconstructed from the data of the best correlated others using quantile mapping (Cannon et al., 2015; Feigenwinter et al., 2018), to provide a reference for robust outlier detection. High-resolution reanalysis series of the parameters measured at CM were also collected as an additional basis for comparison (COSMO-REA2 and COSMO-REA6: Wahl et al., 2017; Bollmeyer et al., 2015; Frank et al., 2018). Due to the large volume of data involved, an automated pre-filtering routine was implemented, based on objective criteria (absolute values, rates of change, comparison with reconstructed series and reanalysis) to mark single values as potential outliers, which were then manually checked. The CM AWS was always processed last in order to be compared to the highest-quality data. After quality check, all gaps in the hourly CM series were filled with the corresponding reconstructed values. The close match of the reconstructed series (Table 3) despite the large elevation differences involved (Table 2) confirms the benefit of the extensive processing described.

The CM AWS does not record series of relative humidity (RH) or cloudiness, which are required within the model input. Thus RH was entirely derived from the other quality-checked time series; cloudiness was reconstructed from the incoming SW radiation at CM when available, and otherwise computed from the incoming LW radiation and observed cloud cover, respectively at Stockhorn and Plateau Rosa. Lapse rates of temperature and pressure – used to extend the AWS record to the gridded model domain – were computed from the difference between CM and the other stations. Further details on the series



**Table 2.** AWS series included in this study. Numbering corresponds to Fig. 1b. X, Y and Z are metric CH1903/LV03 coordinates.  $d_{CG}$  is the horizontal distance to the CG saddle point. Stations 10 and 11 were deployed temporarily for energy-balance studies; permanent stations 3, 4 and 6 were installed between 2006 and 2010, while the others were already operational before the CM AWS. Further AWS information is reported in Mattea (2020).

Id	Name	X [m]	Y [m]	Z [m a.s.l.]	Variables <sup>a</sup>	$d_{CG}$ [m]	Reference
1	Capanna Margherita	634007	86266	4560	T, P, W, S	380	ARPA Piemonte (2020)
2	Gornergrat	626900	92512	3129	T, P, H, W, S, D	9100	MeteoSwiss (2020)
3	Stockhorn	629900	92850	3415	T, H, N, W, S, L	7400	Gruber et al. (2004)
4	Monte Rosa Plattje	629149	89520	2885	T, P, H, W, S	5500	MeteoSwiss (2020)
5	Passo dei Salati	633339	80689	2970	T, H, W	5900	Visit Monte Rosa (2020)
6	Macugnaga Rifugio Zamboni	637094	88977	2075	T, P, H, N, S, R	4200	ARPA Piemonte (2020)
7	Passo del Moro	641664	94075	2820	T, H, R, W, S	11000	ARPA Piemonte (2020)
8	Plateau Rosa	620840	87123	3488	T, P, H, W, C	12900	MeteoAM (2020)
9	Bocchetta delle Pisse	635910	80543	2410	T, N, R, W, S	6400	ARPA Piemonte (2020)
10	Seserjoch	633727	85785	4292	T, H, N, W, S, L, G, F	820	Suter et al. (2004)
11	Colle del Lys	632665	85360	4236	T, H, N, S, W	1700	Rossi et al. (2000a,b)

<sup>a</sup> T: air temperature. P: atmospheric pressure. W: wind speed and direction. S: SW radiation. L: LW radiation. H: relative humidity. D: sunshine duration. N: snow height. C: cloud cover. R: precipitation. G: surface temperature. F: firn temperature. Not all measured variables were used in the study.

**Table 3.** Performance metrics of the simulated CM weather series with respect to the quality-checked hourly measurements.

Variable	RMS	BIAS
Air temperature [ $^{\circ}\text{C}$ ]	1.82	0.02
Barometric pressure [hPa]	1.26	0.00
Wind speed [ $\text{m s}^{-1}$ ]	5.77	-0.08
Global radiation [ $\text{W m}^{-2}$ ]	114	-2

processing can be found in Mattea (2020). Figure 2 shows the final time series of all meteorological parameters assigned to CM and used as model input.

To determine some of the model calibration parameters (Table 4), we also re-analysed data from two additional weather and energy-balance stations (10 and 11 in Table 2), temporarily installed above 4000 m a.s.l. within the ALPCLIM project (Auer et al., 2001). The Seserjoch station operated from September 1998 to October 2000 for the detailed SEB investigations of Suter et al. (2004); the Colle del Lys station (Rossi et al., 2000a,b) was active between 1996 and 2000.

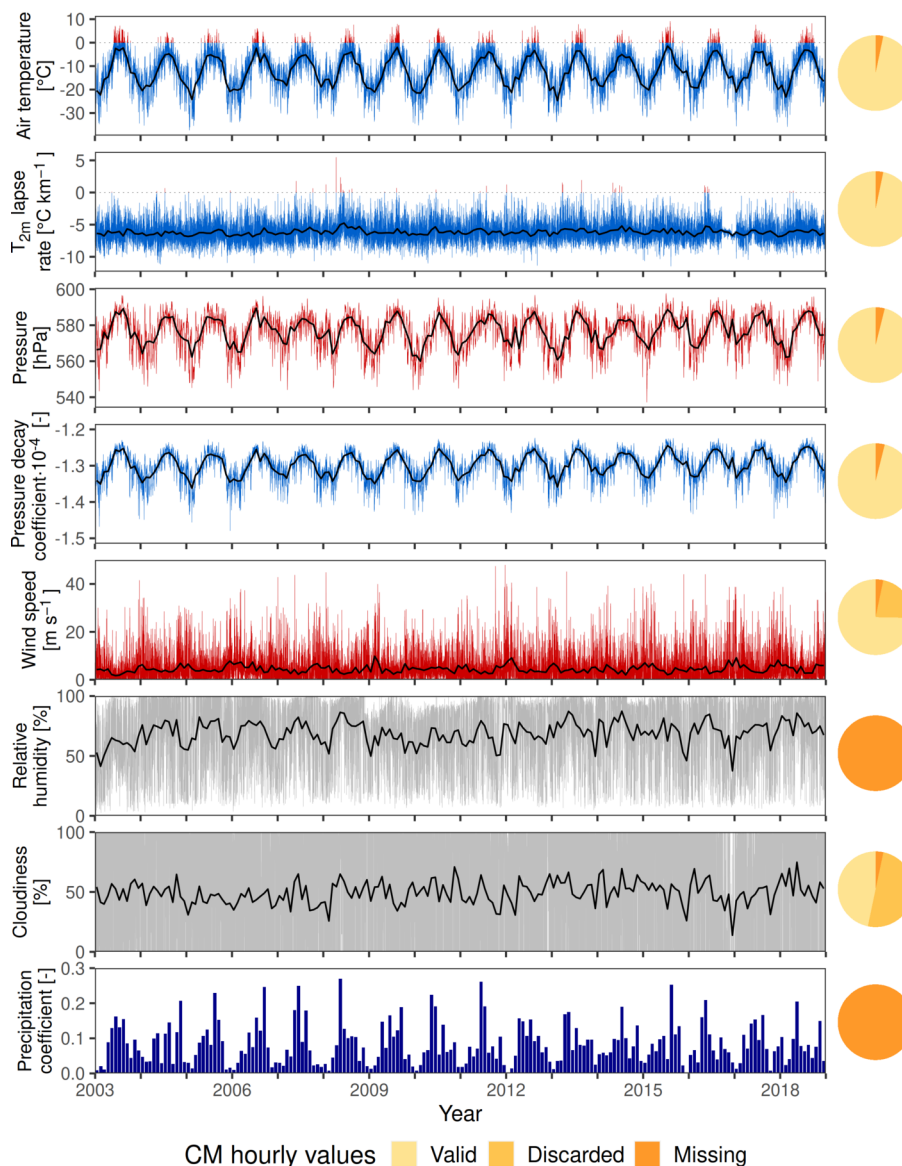


**Figure 2.** Quality-checked and gap-filled hourly weather series used as model input (reference elevation 4560 m a.s.l.). Black lines represent monthly means. For readability, only monthly means are shown for the precipitation down-scaling coefficient (Sect. 3.3). The reduced variability in temperature lapse rates in late 2016 is due to a 4 months data gap, where the series was entirely reconstructed from lower altitude stations. Pie charts show the contribution of the original CM AWS series to the model input. For cloudiness, the contribution is based on values reconstructed from SW radiation measurements. "Discarded" includes values rejected during quality check as well as night-time SW radiation measurements; "missing" includes data gaps and parameters not recorded at CM. All such values were replaced with the reconstructed series.



## 120 2.2 Sub-surface data

For model validation (Sect. 4.1) we used archived firn temperature profiles (Fig. 1a), measured between 2003 and 2018. Beside the CG saddle, we included two profiles from the Grenzletscher slopes and four from Seserjoch. In total, we considered 25 temperature profiles from 18 boreholes, some locations having been measured more than once. Detailed description of the profiles is reported in Hoelzle et al. (2011) and GLAMOS (2017). Earlier information on the deep temperatures (Haeberli and  
125 Funk, 1991) was also used as reference during model set-up (Sect. 3.4).

Moreover, we compiled point measurements of annual accumulation (Fig 3a), derived from layer thicknesses in GPR profiles (Konrad et al., 2013) and from the stake network of Suter and Hoelzle (2002), as well as from archived ice core measurements (densities and annual dating) acquired at CG between 1982 and 2019. In total, 14 core profiles were available; only one (core *Zumsteinkern*, from 1991) is located on the high-accumulation, south-facing Zumsteinspitze slope (Fig. 3a). Description of the  
130 individual cores can be found in Licciulli (2018) and Lier (2018).

Finally, we hand-drilled a 5.5 m core (*unifr-2019*, Fig. 1a) near the CG saddle point on June 25, 2019, analyzing density and stratigraphy in the field. Core description is presented in the appendix.

## 2.3 Topography

The model grid was based on a 20 m digital elevation model (DEM). Due to the Swiss-Italian border crossing the modeling  
135 domain, the DEM was produced by merging the stereo-photogrammetric SwissAlti3D dataset (acquired in 2015 with a vertical accuracy of 1–3 m) on the Swiss side, and the ICE LiDAR digital terrain model (acquired in 2011 with a vertical accuracy of 0.3–0.6 m) on the Italian side (Regione Piemonte, 2011). Elevation mismatch along the border (RMS error of 3.2 m) was corrected via smoothing, to avoid unwanted biases in slope and aspect.

## 3 The coupled energy-balance and firn model (EBFM)

140 The coupled model used in this work was introduced by van Pelt et al. (2012) to simulate mass balance of Nordenskiöldbreen (Svalbard). Driven by a meteorological time series, the model computes energy fluxes on the snow surface: short-wave ( $SW$ ) and long-wave ( $LW$ ) radiation, sensible ( $Q_{SH}$ ) and latent ( $Q_{LH}$ ) turbulent fluxes, heat advection from rainfall ( $Q_{rain}$ ) and heat conduction into the snow or ice ( $Q_g$ ). Then the SEB (Eq. 1) is solved for surface temperature and melt amounts: these, together with the lower boundary condition of geothermal heat flux, drive the sub-surface evolution.

$$145 Q_{melt} = SW_{net} + LW_{net} + Q_{SH} + Q_{LH} + Q_{rain} + Q_g \quad (1)$$

Simulation of surface processes is developed along the lines of Klok and Oerlemans (2002), while the multi-layer sub-surface snow model is based on the SOMARS approach (Simulation Of glacier surface Mass balance And Related sub-surface processes, Greuell and Konzelmann, 1994). In this work, the model version described by van Pelt et al. (2019) was used, with a parametrized water percolation routine simulating preferential flow (Marchenko et al., 2017), and an updated scheme for





150 albedo decay based on Bougamont et al. (2005). This model participated in the firm meltwater Retention Model Intercomparison Project (RetMIP) under the designation "UppsalaUniDeepPerc" (Vandecrux et al., 2020).

In the following we highlight the main EBFM routines and their respective adaptations to the CG setting. The model was originally developed over large, polythermal Arctic glaciers: set-up for a high-alpine cold firm saddle was possible thanks to a rich archive of energy-balance measurements from the Monte Rosa area.

### 155 3.1 Radiative fluxes

The model computes incoming SW radiation as

$$SW_{in}(x, y) = TOA_{shaded}(x, y) t_{rg} t_w t_a t_{cl} \quad (2)$$

$$t_{cl}(n) = 1 - an - bn^2, \quad (3)$$

160 where  $TOA_{shaded}(x, y)$  is the unattenuated top-of-atmosphere radiation corrected for topographic shading,  $t_{rg}$ ,  $t_w$ ,  $t_a$  and  $t_{cl}$  gaseous, water vapor, aerosol and cloud transmissivities,  $n$  fractional cloud cover, and  $a$  and  $b$  calibration parameters. Values for  $a$  and  $b$  (Table 4) were derived from Greuell et al. (1997) as calibrated in high-alpine terrain, compared to the EBFM defaults which were tuned from measurements in the Arctic. The choice was supported by a distribution analysis of the incoming SW flux, measured at the CM AWS under overcast sky conditions.

165 Reflected SW radiation is controlled by a broadband, isotropic surface albedo (Eq. 4). Albedo evolution is modeled after Oerlemans and Knap (1998) as an exponentially decaying function of time since last significant snowfall (Eq. 5), bounded by constant values for fresh snow and firn. Decay time-scale is a function of snow surface temperature (Eq. 6) to account for slower metamorphism in cold conditions (Bougamont et al., 2005; van Pelt et al., 2019):

$$SW_{out} = \alpha_{snow} SW_{in} \quad (4)$$

$$\alpha_{snow}(t) = \alpha_{firn} + (\alpha_{fresh} - \alpha_{firn}) e^{-\frac{t}{t^*}} \quad (5)$$

$$170 \quad t^*(T) = \begin{cases} t_{wet}^* & T = 0 \text{ } ^\circ\text{C} \\ t_{dry}^* + K \max(T, T_{max, t^*}) & T < 0 \text{ } ^\circ\text{C}, \end{cases} \quad (6)$$

where  $t^*$  is the computed albedo decay time-scale,  $t_{wet}^*$  ( $t_{dry}^*$ ) time-scale for a melting (dry) surface at 0 °C,  $K$  a calibration parameter,  $T$  snow surface temperature and  $T_{max, t^*}$  a temperature cut-off value for decay slow-down. Values for these parameters (Table 4) were estimated from a new analysis of albedo evolution, measured at the Seserjoch and Colle del Lys stations respectively in 1999 and between 1996 and 2000.



**Table 4.** EBFM parameters considered for calibration. Additional model parameters not listed here were kept at the default value (van Pelt et al., 2012; van Pelt and Kohler, 2015; van Pelt et al., 2019).

Parameter	Definition	Unit	Value	Source
$a$	Cloud SW transmissivity coefficient	-	0.233	Greuell et al. (1997), verified with CM AWS data
$b$	Cloud SW transmissivity coefficient	-	0.415	Greuell et al. (1997), verified with CM AWS data
$\alpha_{fresh}$	Fresh snow albedo	-	0.83	Tuned from Seserjoch and Colle del Lys radiation
$\alpha_{firn}$	Firn albedo	-	0.52	EBFM default (van Pelt and Kohler, 2015)
$t_{wet}^*$	Decay time-scale (melting snow surface)	d	10	Tuned from Seserjoch and Colle del Lys radiation
$t_{dry}^*$	Decay time-scale (dry snow surface at 0 °C)	d	30	EBFM default (Bougamont et al., 2005)
$K$	Increase of $t_{dry}^*$ at negative temperatures	d °C <sup>-1</sup>	14	Tuned from Seserjoch and Colle del Lys radiation
$T_{max,t^*}$	Temperatures cut-off for the $t_{dry}^*$ increase	°C	-10	EBFM default (Reijmer et al., 2005)
$b$	Constant in LW emission formula	-	0.420	Tuned from Seserjoch LW measurements
$e_{cl}$	Clouds emissivity	-	0.960	Tuned from Seserjoch LW measurements
$z_0$	Surface roughness length	m	0.001	Suter et al. (2004) from Seserjoch wind profiles
$Q_{ground}$	Geothermal flux	W m <sup>-2</sup>	0.040	Lüthi and Funk (2001) from CG boreholes
$\rho_{fresh}$	Fresh snow density	kg m <sup>-3</sup>	350	Klok and Oerlemans (2002)
$z_{lim}$	Characteristic depth of meltwater infiltration	m	4	Tuned to CG 20 m firn temperatures

175 Incoming LW radiation is computed with the Stefan-Boltzmann law for grey-body radiation (Eq. 7); sky emissivity is modeled after Konzelmann et al. (1994) as a function of cloud cover, air temperature and humidity (Eqs. 8 and 9):

$$LW_{in} = e\sigma T^4 \quad (7)$$

$$e = e_{cs}(1 - n^2) + e_{cl}n^2 \quad (8)$$

$$e_{cs} = 0.23 + b \left( \frac{VP}{T} \right)^{0.125}, \quad (9)$$

180 where  $e_{cs}$  is clear-sky emissivity,  $b$  a calibration parameter,  $VP$  vapor pressure,  $T$  air temperature,  $e$  sky emissivity,  $n$  fractional cloud cover and  $e_{cl}$  cloud emissivity. Parameters  $b$  and  $e_{cl}$  were estimated for CG from radiation measurements at Seserjoch.

### 3.2 Turbulent heat fluxes

In the EBFM, turbulent heat exchange is modeled with the glacier katabatic wind parametrization of Oerlemans and Grisogono (2002). This was developed with a focus on large valley glaciers; notably, it computes heat fluxes which are independent on the ambient wind field, since wind speeds are estimated from the katabatic flow model (Oerlemans and Grisogono, 2002). This was deemed inadequate for a high-alpine, wind-exposed saddle: thus the EBFM computation of turbulent heat exchange was re-implemented, following the bulk aerodynamic equations of Essery and Etchevers (2004). These were chosen due to their operational simplicity, allowing calculation of turbulent fluxes from a single measurement level of wind speeds. The fluxes are



computed as

$$190 \quad Q_{SH} = \rho_a c_p C_h V_1 (T_1 - T_s) \quad (10)$$

$$Q_{LH} = \rho_a L_{s,v} C_h V_1 (q_1 - q_s), \quad (11)$$

where  $\rho_a$  is air density,  $c_p$  specific heat of dry air,  $V$  wind speed,  $T$  air temperature,  $L_{s,v}$  latent heat of sublimation or vaporization (chosen depending on the modeled surface temperature),  $q$  specific humidity, and the  $s$  and 1 subscripts refer respectively to the snow surface and the measurement level (2 m). Exchange coefficient  $C_h$  is defined as

$$195 \quad C_h = C_{hn} f_h, \quad (12)$$

where  $C_{hn}$  is the value under neutral conditions and  $f_h$  a correction for atmospheric stability, expressed in terms of the bulk Richardson number  $Ri_B$ :

$$C_{hn} = k^2 \left( \log \left( \frac{z_1}{z_0} \right) \right)^{-2} \quad (13)$$

$$f_h = \begin{cases} (1 + 10Ri_B)^{-1} & Ri_B \geq 0 \text{ (stable)} \\ 1 - 10Ri_B \left( 1 + 10C_{hn} \frac{\sqrt{-Ri_B}}{f_z} \right)^{-1} & Ri_B < 0 \text{ (unstable)} \end{cases} \quad (14)$$

$$200 \quad Ri_B = \frac{gz_1}{V_1^2} \left( \frac{T_1 - T_s}{T_1} + \frac{q_1 - q_s}{q_1 + \epsilon(1 - \epsilon)^{-1}} \right) \quad (15)$$

$$f_z = \frac{1}{4} \left( \frac{z_0}{z_1} \right)^{0.5}. \quad (16)$$

Here,  $k$  is the von Kármán constant,  $z_1$  the measurement level,  $z_0$  the surface roughness length,  $g$  the gravity acceleration, and  $\epsilon$  the ratio of molecular weights for water and dry air.

### 3.3 Precipitation model

205 The model precipitation routine was adapted to reproduce the extreme spatial gradient of snow accumulation distinctive of the site (Sect. 1). Since the EBFM does not include a blowing snow routine, the simple model of linear precipitation rates with altitude (van Pelt et al., 2019) was replaced by a gridded precipitation time series, already corrected for snow lost to wind scouring. This was computed with a three-phase anomaly method inspired from New et al. (2000), by combining a fixed climatological grid, an annual anomaly series, and a temporal down-scaling coefficient. Specifically, for grid cell  $(x, y)$ , at  
 210 simulation time-step  $t$ , in year  $i$ , precipitation was expressed as

$$P(x, y, t) = C(x, y)A(i)D(t), \quad (17)$$

where  $C$  is the long-term annual accumulation climatology,  $A$  the domain-wide annual anomaly, and  $D$  the down-scaling coefficient. The main assumption of the method is that spatial patterns of relative accumulation do not change over time. The climatological grid  $C$  was assembled by interpolating point values of long-term net accumulation, estimated from the snow



215 mass of dated firn cores and from the mean layer thickness in GPR profiles (Fig. 3a). To extend data coverage and reduce the occurrence of extrapolation, stake measurements from Suter and Hoelzle (2002) were also used in the western and southern domain regions. Accumulation measured at each stake over a single year was re-scaled to a mean annual estimate by using the overlaps with firn cores and GPR points.

For annual anomalies  $A$ , the multiplicative snow mass anomaly of the *KCC* deep core (Bohleber et al., 2018) was found to  
220 be moderately anti-correlated with wind speed measured at the CM AWS (Fig. 3b). Linear fit over 9 annual data points yielded the formulation

$$A = 1.46 - 0.21\bar{V} \quad (18)$$

where  $A$  is core snow mass anomaly and  $\bar{V}$  the median wind speed observed at CM over the corresponding year. Anomaly from the *KCC* core was then applied to the whole domain.

225 Finally, the down-scaling coefficients  $D$  were computed by normalizing to a unit sum each year of hourly precipitation, averaged over the three closest rain gauges (Passo Monte Moro, Bocchetta delle Pisse and Rifugio Zamboni: Fig. 1b, Table 2). Equation 17 produces an hourly series of gridded precipitation (already corrected for wind erosion) which was used to force the EBFM.

### 3.4 Water infiltration

230 The EBFM features a parametrized water infiltration routine, which routes any liquid water from the snow surface towards depth, instantly and according to a constant vertical distribution (Marchenko et al., 2017), as long as the modeled near-surface layers are not impermeable. Water at depth can then refreeze, be held by **capillary forces as irreducible water**, or form slush layers which drain gradually (van Pelt et al., 2012). In this study, the water vertical distribution was chosen to follow the normal law; the maximum depth  $z_{lim}$  was tuned to a value of 4 m, to match the firn temperature of the CG saddle point at a depth of  
235 20 m (Haeberli and Funk, 1991).

### 3.5 Model initialisation

The model grid was initialized to steady state conditions by looping eight times over the 2004–2011 weather input: the period was selected to exclude the extreme melt year of 2003 and the increasing temperature warming of the 2010s. Then two main model runs were performed, with 20 m / 1 h and 100 m / 3 h spatio-temporal resolution. The coarser version was introduced to  
240 decrease the large computational volume of sub-surface investigations (Fig. 6) and to perform simple sensitivity experiments. On the depth axis, the model grid included 250 layers up to 10 cm thick, for an effective modeling depth of about 20 m (EBFM layers follow a Lagrangian discretization to prevent numerical diffusion, so their thickness is variable over time: van Pelt et al., 2019).

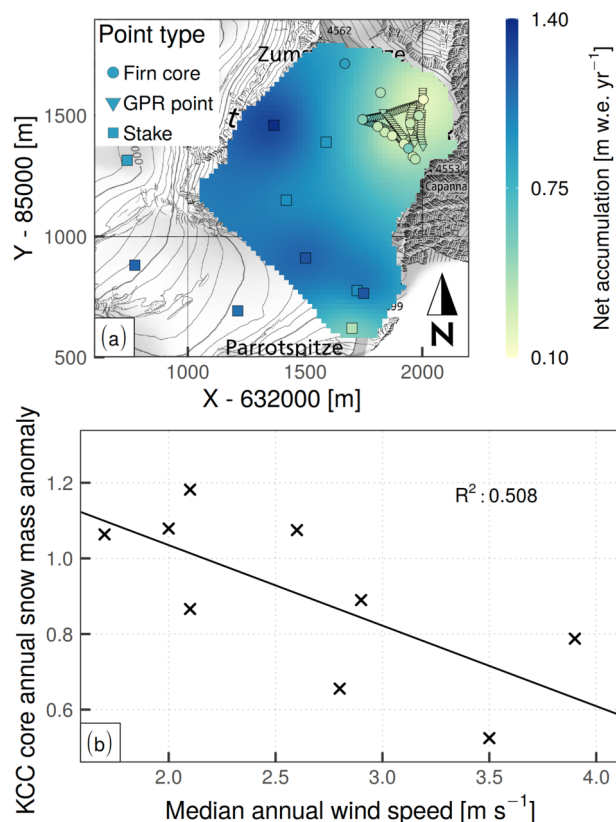


**Figure 3.** (a) Long-term net annual accumulation climatology at CG, serving as spatial component for the distributed accumulation model. Dense point sequences in the north-east were derived from GPR profiles. X and Y are metric CH1903/LV03 coordinates. Topographic map source: Federal Office of Topography swisstopo. (b) Linear fit of annual snow mass anomaly at core KCC versus median annual wind speed at the CM AWS.

## 4 Results

245 The EBFM computes and logs a wide variety of surface and sub-surface variables. In the following, we focus on firn temperatures and melt amounts as relevant descriptors of current cold firn evolution. For these variables, a conspicuous archive of field measurements and model estimates exists at CG, allowing verification and comparison of our results.

### 4.1 Firn temperatures

250 Comparison of modeled firn temperatures to measured borehole profiles (Table 5, Fig. 4 and 5) shows that most model deviations are similar in magnitude to the spatial variability of firn temperatures. Indeed, profiles CG08-1/08 and CG08-2/08 (acquired in the flat region, on the same day and within a radius of 20 m: Fig. 4e/f) report measured temperature differences in excess of 2 °C at all depths. Model residuals show a clear spatial pattern: simulated profiles tend to be too cold on shaded,



north-facing slopes, and too warm in the flat or south-facing regions of CG and Seserjoch. Moreover, model biases appear to be maintained over time for boreholes with repeated measurements (e.g., CG05-1 and CG13-1).

**Table 5.** Performance metrics of the modeled firn temperatures.

Model run	Profiles	RMS [ $^{\circ}\text{C}$ ]	BIAS [ $^{\circ}\text{C}$ ]
20 m / 1 h	CG only	1.3	-0.4
	All	1.4	-0.3
100 m / 3 h	CG only	1.4	0.0
	All	1.6	0.1

255 The time series of modeled firn temperatures (Fig. 6) shows large differences over rather small distances at the CG saddle, depending on surface aspect. Still, relative annual deviations are consistent across locations. The annual cycle on average reaches an amplitude of  $40^{\circ}\text{C}$  at the snow surface and is fully damped at a depth of 20 m.

The model simulates the frequent summer occurrence of infiltration and refreezing, reflected in sudden near-surface warming events (inset in Fig. 6). Magnitude of these events shows a high variability, with especially large heat amounts simulated in the summers of 2003, 2008, 2015 and 2017. With more meltwater refreezing, the sun-exposed ZS slope commonly shows sustained near-melting temperatures in the topmost 4 m; conversely, these conditions almost never appear at the shaded SK location.

260 A slight positive temperature anomaly can be seen at depth after the extreme melt year of 2015, persisting over the following years despite non-record melt amounts. Across the CG saddle, overall firn warming modeled at 20 m depth over 2003–2018 amounts to  $0.64\text{--}0.75^{\circ}\text{C}$ . At the saddle point, this corresponds to a rate of  $0.44^{\circ}\text{C}$  per decade.

## 4.2 Melt amounts and dynamics

Modeled mean annual melt amounts have an extreme spatial variability (Fig. 7), broadly reflecting surface elevation, slope and aspect. Values increase from less than  $1\text{ cm w.e. yr}^{-1}$  on the steepest slopes of the Signalkuppe, to  $17\text{ cm w.e. yr}^{-1}$  at the saddle point, and about  $23\text{ cm w.e. yr}^{-1}$  on the Zumsteinspitze slope. Even higher melt amounts, exceeding  $30\text{ cm w.e. yr}^{-1}$ , are simulated for the lower elevation Grenzgletscher slopes (towards the western border of the domain) and for Seserjoch. Grid average is  $21\text{ cm w.e. yr}^{-1}$ . Within the overall energy balance, melt represents a relatively minor component (Fig. 8): the largest mean monthly contribution, in August, is well below 10 %, and in every month sublimation is a more effective energy sink than melt. Still, in the NE domain region – where wind scouring is strongest – annual melt amounts correspond to a significant fraction of net accumulation (Fig. 3a). With regard to temporal patterns, the entire surface was found to always refreeze at night over the modeled period. Moreover, no melt is simulated between November and March, with only minor amounts in April and October (Fig. 8).

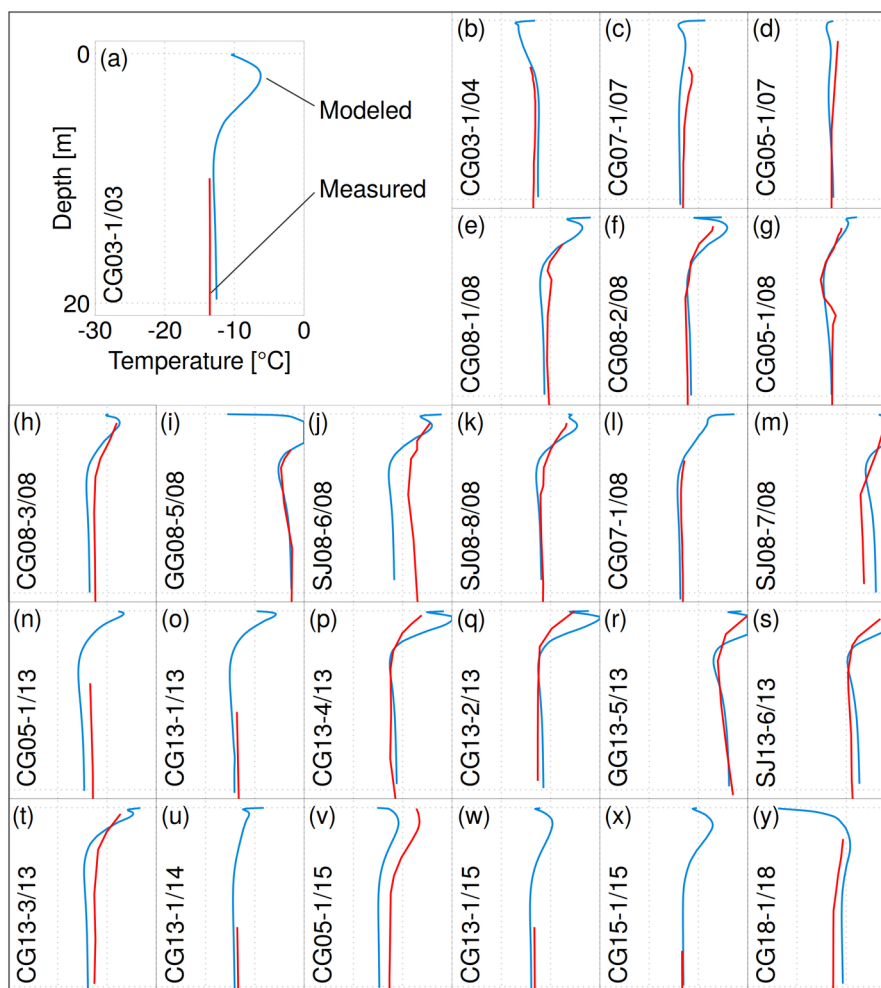


**Figure 4.** Measured and modeled borehole temperature profiles, sorted chronologically. Axes range is the same in all plots. The bottom depth of 20 m corresponds to the deepest simulated values and to the depth of zero amplitude of the annual cycle. Profile codes follow the scheme XXYY-Z/WW, with XX location code, YY borehole year, Z borehole number, and WW year of the profile measurement (Hoelzle et al., 2011; GLAMOS, 2017). Letter codes correspond to Fig. 5.

Despite the large spatial heterogeneity, and an inter-annual variability exceeding 50 %, a common trend of melt increase could be detected in the annual time series (Fig. 9): the fitted slope ranges between  $(3 \pm 2)$  and  $(4 \pm 3)$  mm w.e.  $\text{yr}^{-2}$  across the saddle. While the trend is somewhat masked by the 2003 extreme melt year at the very beginning, it becomes statistically significant over the rest of the period.

The EBFM shows a marked tendency towards small melt amounts: frequency of modeled melt events decays exponentially with their magnitude (Fig. 10a), and a significant fraction of total melt amounts is contributed by micro-melt events under 4 mm w.e. (Fig. 10b).

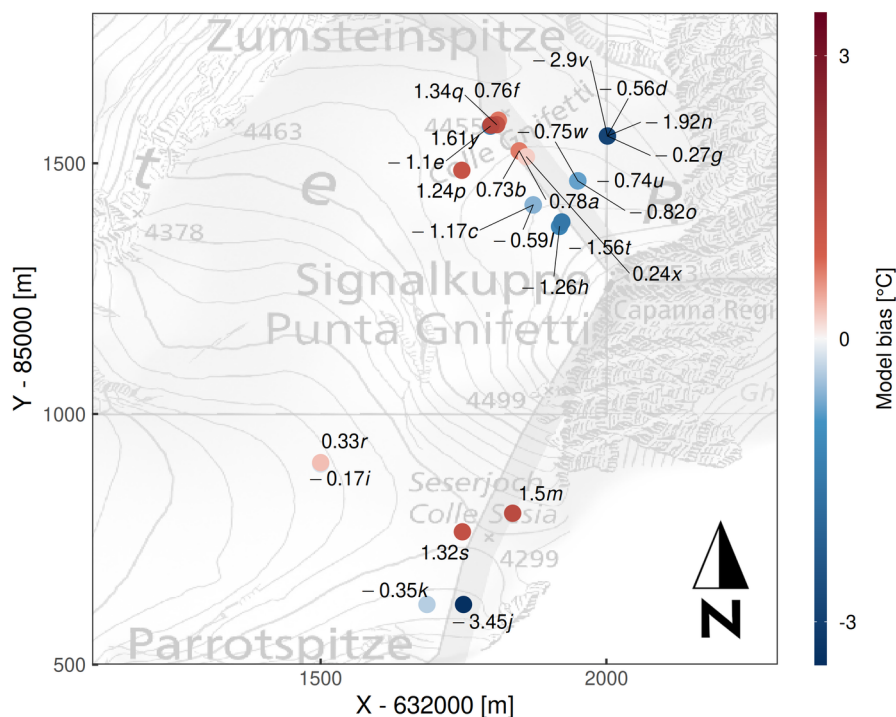


**Figure 5.** Map of mean residuals of modeled borehole temperature profiles (20 m grid, 1 h time-step). Letter codes correspond to Fig. 4. X and Y are metric CH1903/LV03 coordinates. Topographic map source: Federal Office of Topography swisstopo.

Investigation of the weather conditions leading to melt occurrence (Fig. 11) reveals the relationship between weather variables and surface melt. Air temperature provides a critical control over melt rates and total amounts, unlike cloud cover which appears to have almost no effect (Fig. 11a/b). The majority of melt happens under clear-sky conditions, and significant amounts are simulated between  $-5$  and  $0$  °C (Fig. 11b). Non-zero (though minimal) melt amounts are modeled down to air temperatures of  $-7$  °C, under clear skies and moderate to high humidity. Conversely, in very dry conditions (Fig. 11c/d) sublimation losses hinder melt even at slightly positive temperatures. Finally, wind speed appears to have a minor effect on long-term mean melt rates, slightly decreasing the likelihood of melt under high winds (Fig. 11e/f).

## 5 Discussion

At CG, the repeated, long-term investigations enable interpretation of the model output against a rich literature background. The following sections evaluate and put into context the model results for firn temperatures, meltwater infiltration and refreezing, as well as melt amounts.



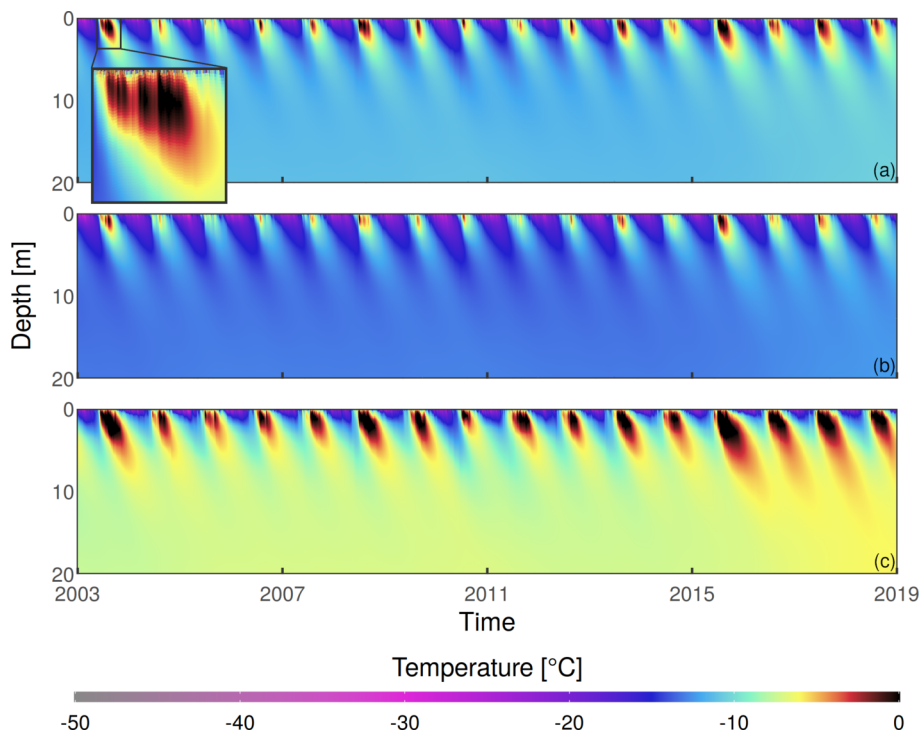


**Figure 6.** Time-depth plots of modeled firn temperatures at (a) CG, (b) SK and (c) ZS (map in Fig. 1a). 100 m grid, 3 h time-step. Inset shows 2003 summer temperatures down to 3.5 m depth.

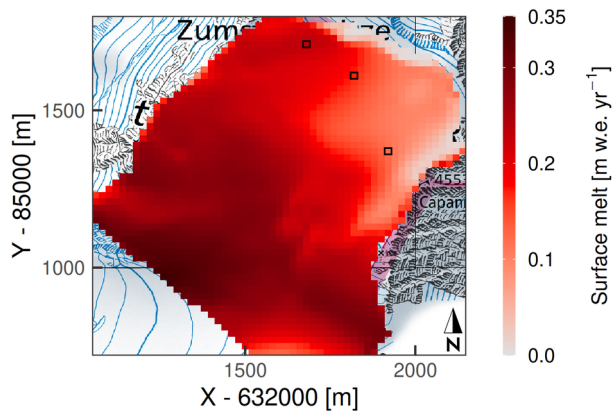


**Figure 7.** Mean (2003-2018) modeled annual melt amounts (20 m grid, 1 h time-step). Marked cells correspond to the representative points of Fig. 1a. X and Y are metric CH1903/LV03 coordinates. Topographic map source: Federal Office of Topography swisstopo.

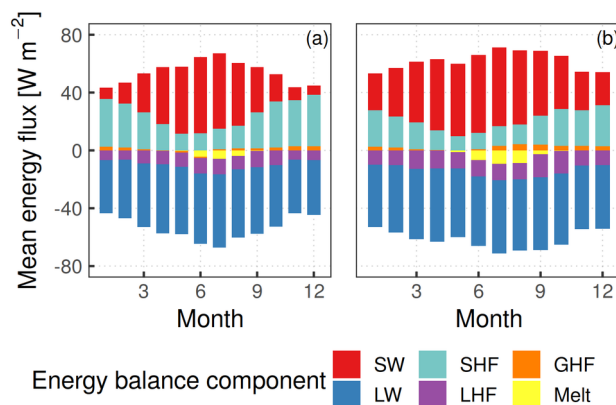


**Figure 8.** Mean (2003–2018) monthly distribution of modeled energy balance components at (a) SK and (b) ZS. 20 m grid, 1 h time-step. Distribution of fluxes at CG (not shown) is intermediate between the two.

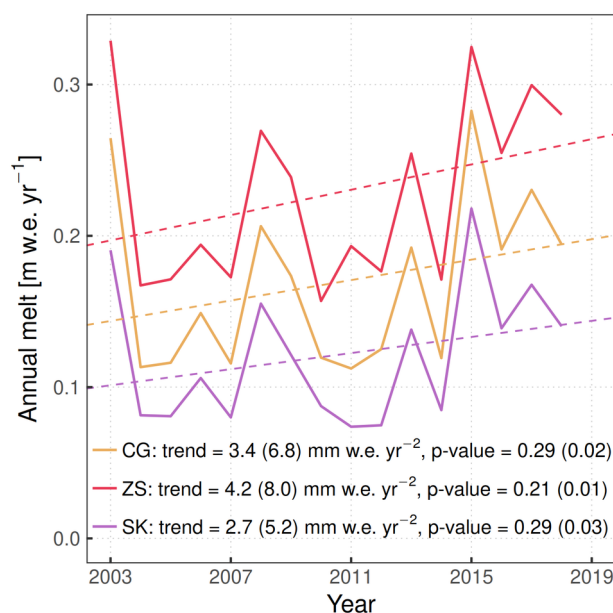


**Figure 9.** Time series of modeled annual melt amounts at three representative grid cells (solid lines; CG: saddle point, SK: Signalkuppe slope, ZS: Zumsteinspitze slope). Linear least-squares fits (each including  $n = 16$  annual values) are shown as dashed lines. Reported annual melt trends and corresponding p-values are computed both on the whole 2003–2018 modeling period (first number), and excluding the extreme melt year of 2003 (second number, in parentheses). 20 m grid resolution, 1 h time-step.

## 295 5.1 Firn temperatures

The EBFM shows considerable potential at simulating cold firn. In addition to reproducing individual borehole profiles, the model confirms broader patterns such as the strong firn temperature gradient towards the Grenzgleitscher slopes (Suter and

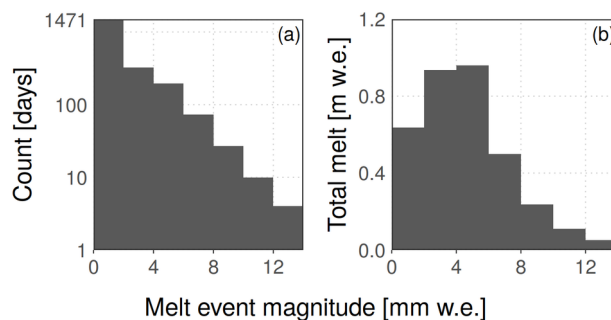


**Figure 10.** (a) Distribution of magnitudes of modeled melt events (defined as total daily melt amounts). Y-axis is logarithmic. (b) Cumulative melt amounts sorted by the magnitude of contributing melt events. Melt amount for each event is averaged over the whole domain of Fig. 7. 20 m grid resolution, 1 h time-step.

Hoelzle, 2002) and the depth of zero annual temperature oscillation, at about 20 m (Hoelzle et al., 2011). This last observation indicates a realistic simulation of heat conduction.

300 The spatial distribution of model residuals (Fig. 5) could be affected by the lack in the modeled SEB of radiation reflected from the surrounding terrain. This process is expected to induce a net energy transfer from the more sun-exposed cells towards the more shaded ones, which could partially re-balance the aspect dependence of model residuals.

In addition, boreholes with positive model bias are often simulated with too strong near-surface temperature gradients, leading to sharp positive deviations in the profile near the surface (e.g., Fig. 4f/k/p/q). Such a behavior suggests too deep  
305 refreezing is occurring in the simulation, which could be linked to the parametrized preferential infiltration routine (Sect. 3.4). Indeed, below a depth of 0–4 m (where refreezing is occurring) the simulation appears to be unbiased at most locations.

Model under-estimation of firm temperatures appears to correlate with the lowest mean annual accumulation values (Fig. 3a and 5). At these locations wind scouring is strongest, and melt amounts represent a significant fraction of net annual accumulation. Simple sensitivity tests showed that the simulation of profiles at borehole location CG05-1 improves substantially by  
310 forcing increased precipitation amounts. This suggests that the accumulation model – which computes precipitation amounts already corrected for losses from wind scouring – may be problematic whenever melt totals approach the value of net accumulation. Indeed, accumulation at CG results from summer precipitation events (Sect. 1), but modeled precipitation is distributed more evenly throughout the year, as it is based on weather station measurements (Sect. 3.3). Thus we expect modeled precipitation to be under-estimated in summer compared to the actual accumulation. As such, in summer modeled melt can temporarily  
315 approach (or even locally exceed) the low accumulated snow amounts. Then the parametrized percolation would generate dense, thick firm layers: their limited refreezing capacity could reduce the heat release at depth during subsequent melt events, inducing under-estimation of the englacial temperatures.


Among past modeling efforts at CG, both Lüthi and Funk (2001) and Suter (2002) formulated independent predictions for firm temperatures evolution by 2020. As the target time frame for verification is reached, a major limitation of their modeled  
320 scenarios is found in the expected magnitude of atmospheric warming: while they assumed linear air temperature increases

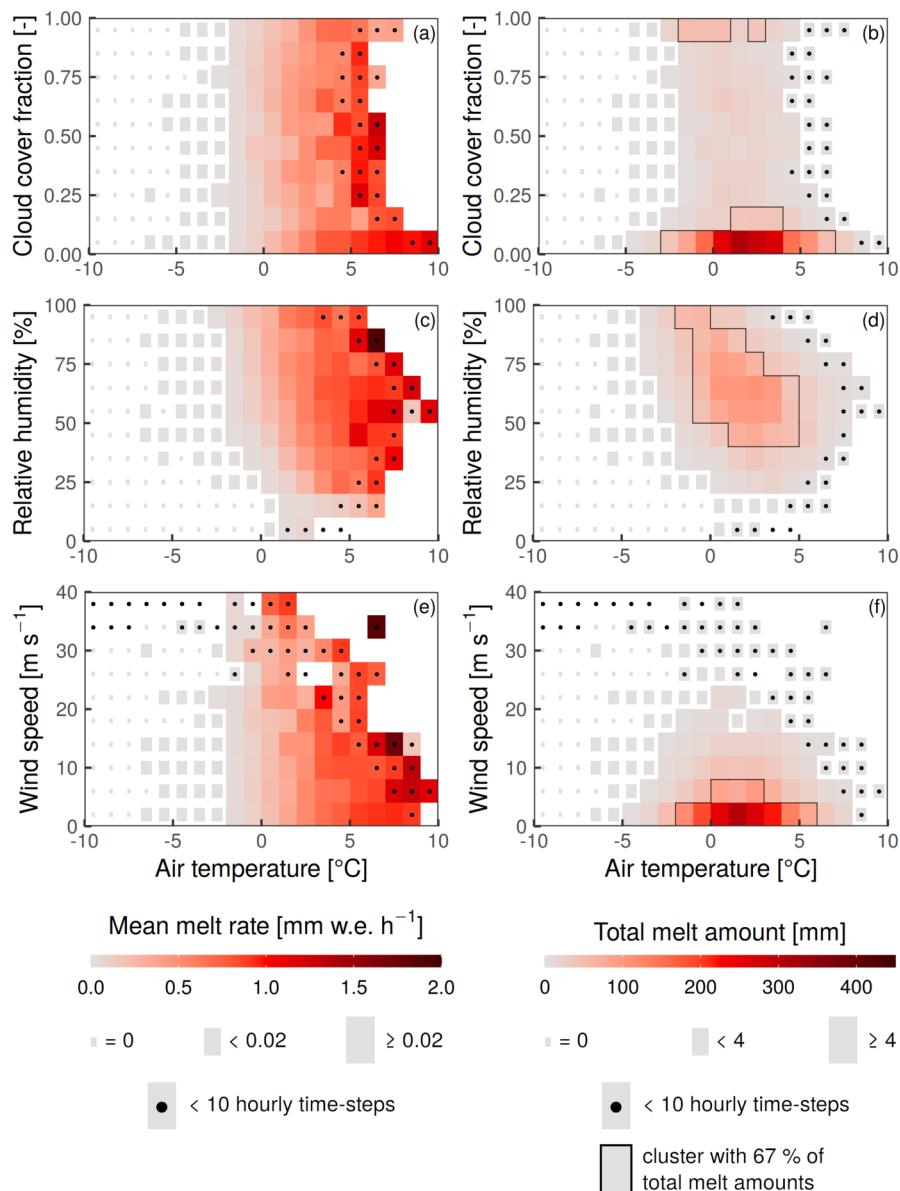



**Figure 11.** Mean melt rates (left) and cumulative melt amounts (right) modeled over 2003–2018 at the CG saddle point (20 m grid / 1 h time-step), sorted according to the respective weather conditions: air temperature and (a–b) cloud cover, (c–d) relative humidity, (e–f) wind speed. Tiles of weather conditions not encountered in the input series are not drawn.

by respectively 0.4 and 0.45  $^{\circ}\text{C}$  between 2000 and 2020, the fitted trend at the CM AWS (series in Fig. 2) amounts to 0.05  $^{\circ}\text{C yr}^{-2}$ , corresponding to a much stronger warming of 1  $^{\circ}\text{C}$  over the period. For the CG saddle region, the two studies predict firn temperature increases at 18 m by 0.42 and 1.06  $^{\circ}\text{C}$  respectively, between 2000 and 2020. By comparison, the EBFM



simulates 0.70 °C of warming between 2003 and 2018, which can be uniformly rescaled over 2000–2020 to 0.88 °C. Such a  
325 firm warming is consistent with the results of the two studies, but lower when compared to the assumed air temperature increase.  
A contributing factor could be the EBFM spin-up: temperatures were initialized with repeated model runs over 2004–2011,  
thus the initial grid at all depths is in equilibrium with the mean forcing over that period. By contrast, an adjustment time of  
2–4 years is to be expected at the considered depth (Hoelzle et al., 2011). Therefore at the beginning of the simulation the  
EBFM may be slightly over-estimating deep firn temperatures (Fig. 4a/b), resulting in a lower trend for 2003–2018. 

## 330 5.2 Meltwater infiltration

A key parameter used for model set-up is the percolation depth  $z_{lim}$ , which defines the maximum depth reached by infiltrated  
meltwater through preferential flow. In cold firn such a parameter is crucial: simulated firn temperatures (Fig. 6) indicate that all  
meltwater can be expected to refreeze not far from the initial location (controlled by the parametrized vertical distribution: Sect.  
3.4). Thus  $z_{lim}$  effectively determines not only the initial meltwater distribution, but also the depth of refreezing heat release.  
335 The calibrated value of 4 m, together with the Gaussian vertical distribution, correspond to a mean preferential percolation  
depth of 1.06 m. Unfortunately, in situ quantitative measurements of infiltration depths are scarce and mostly indirect. Evidence  
from winter snow packs and glacier accumulation areas shows that percolation and refreezing are strongly dependent on the  
meltwater supply amounts and rates (Marchenko et al., 2017), the temperature of the firn matrix (Koerner, 1970) and its  
stratigraphy (Illangasekare et al., 1990), notably affected by the previous history of infiltration and refreezing. An obvious  
340 consequence is the increase of percolation depths over the melting season (Marchenko et al., 2017). At CG, Alean et al. (1983)  
observed slight melting but no meltwater percolation during a warm spell in summer 1981. Suter (2002) attempted to directly  
track meltwater refreezing by continuously logging a temperature profile at Seserjoch in 1999, but the setup failed before the  
onset of summer melt. Hoelzle et al. (2011) reported evidence for increasing infiltration depths, indicating (at Seserjoch and on  
the Grenzgletscher slopes) a transition to a percolation regime spanning several annual firn layers. By contrast, the stratigraphy  
345 of core *unifr-2019* (Fig. A1) revealed dry firn layers interspersed with thin ice crusts, suggesting small amounts of infiltration  
and refreezing, except for a thick, ice-rich layer at 4.5 m depth. Therefore in our simulation we consider  $z_{lim}$  more as a tuning  
parameter than a realistic percolation depth 

Stratigraphy of the firn core points to a shortcoming of the subsurface model: meltwater distributed in cold firn along the  
parametrized vertical profile usually refreezes in place, producing a diluted density increase in the simulation. Instead, distinct  
350 ice layers are known to form at depth after preferential percolation, affecting the mechanical, hydrological and thermodynamical  
properties of the snow pack (Quéno et al., 2020). In the present EBFM formulation, such ice layers would not appear even  
with a very fine model grid. Refreezing after parametrized infiltration also distributes heat instantly over a fixed, large vertical  
extent, resulting in unrealistic, frequent warm pulses at depth after each melt event – no matter how small (inset in Fig. 6).  
These observations indicate the need for a physically based percolation routine in the EBFM, accounting for the time evolution  
355 of  $z_{lim}$  and its dependence on snow density and stratigraphy.



### 5.3 Melt amounts

Modeled melt amounts can be compared to the amount of refrozen ice observed in core *unifr-2019* (Fig. A1). According to the computed climatology (Fig. 3a), the core location has a mean long-term accumulation of about 50 cm w.e. yr<sup>-1</sup>: thus the 5.5 m core should span an estimated period of about 5–6 years (with a fairly large uncertainty due to the inter-annual accumulation variability). The model predicts about 85–100 cm w.e. of melt over such a time span (Fig. 7), while the core was found to contain only 31 cm of ice layers. Some observations can be brought forward to put the apparent discrepancy into context.

First, refrozen ice amounts recorded in the core are affected by repeated cycles of melt-refreeze. Indeed, the very small amounts of meltwater produced during less intense (but rather frequent: Fig. 10) melt events can be expected to refreeze in the very first snow centimeters. Then any subsequent melt occurring before the next snowfall would affect the same ice surface, contributing to total melt amounts but without significant increases in ice layer thickness. Such surface crusts of relatively impermeable ice have already been observed at CG (e.g., Lier, 2018). Since melt mostly happens in clustered patterns (almost only in summer and within a specific set of weather conditions: Fig. 8 and 11), contribution of repeated melt-refreeze cycles could potentially be very large.

With daily melt amounts often close to the size of single crystals (Fig. 10a), it is suggested that detection of some refrozen forms would require a resolution not achieved during our field analysis. Investigations of such minimal melt processes are very limited in the literature. Still, Das and Alley (2005) performed hot-box experiments on the formation of thin refreeze layers in Antarctic snow, finding that a profile resolution of 1 mm was necessary to capture small-scale melt processes. Moreover, in their experiments the wetted and refrozen snow next to melt layers did not show any type of melt feature detectable in firm core stratigraphy (Das and Alley, 2005), possibly enabling some refrozen layers to remain undetected. The possibility of an overlooked vertical ice gland embedded in our core also cannot be ruled out (measured core sections were not broken up after analysis). In fact, the presence of undetected ice would be consistent with the high density variability encountered in the core profile (Fig. A1). Still, this observation could also be linked to wind compaction, and its interplay with wind erosion exposing older, denser snow.

An estimation of refreezing amounts from profile density anomalies was proposed by Lier (2018), using several new and archived cores in the CG area. The method involved sizable uncertainties due to a poorly constrained surface density value. At the *Sattelkern* and *Zumsteinkern* cores (respectively at the saddle point and on the south-facing slope), estimated refreezing rates are respectively in the 1–13 and 3–33 cm ice yr<sup>-1</sup> ranges (Lier, 2018). The EBFM predicts approximately 19 and 25 cm ice yr<sup>-1</sup> of melt. On the shaded Signalkuppe flank, values span the range 0–15 cm ice yr<sup>-1</sup> from multiple cores; the EBFM result over the same region is between 5 and 12 cm ice yr<sup>-1</sup> of melt. Considering the very strong inter-annual variability of melt amounts (Fig. 9), the results are largely compatible.

The significant melt amounts modeled at sub-freezing temperatures suggest reconsideration of degree-day models for simulating melt at high-alpine (and possibly high-latitude) locations. This is consistent with the findings of Suter et al. (2004) at Seserjoch, who observed several surface melt events but no days with positive mean temperatures over the whole 1999 summer. Indeed, laboratory experiments by Beck et al. (1988) revealed the occurrence of melt already at -4 °C with 475 W m<sup>-2</sup> of



390 incoming SW radiation. At the CM AWS values in excess of  $1000 \text{ W m}^{-2}$  are a common summer occurrence, supporting the  
plausibility of melt under even colder conditions (Fig. 11). From a theoretical perspective, Kuhn (1987) analytically explored a  
standard SEB equation (neglecting sub-surface heat conduction), in relation to common weather situations on an alpine glacier.  
The conclusion was that melt onset likely happens at air temperatures between  $-10$  and  $+10 \text{ }^\circ\text{C}$ , very much comparable to our  
results.

## 395 6 Conclusions and outlook

This work marked a first effort to apply a coupled, high-resolution EBFM to alpine cold firn, within a multi-year simulation  
forced with extensively processed meteorological data, acquired at high altitude and in closest vicinity of the study site. In both  
cold and near-temperate conditions, the model can achieve promising results for firn temperatures, comparable in accuracy to  
the spatial variability of the measurements. Therefore the EBFM can be deemed suitable for further investigations of future  
400 cold firn evolution, based on localized climate scenarios.

At CG, our results corroborate earlier observations on the spatial patterns of surface melt and the trends of deep temperatures.  
A previously unreported feature in melt dynamics is the occurrence of micro-melt events, with daily amounts below  $4 \text{ mm w.e.}$ :  
these remain difficult to detect, but our analysis hints at a possibly significant impact on melt totals and firn temperatures, hence  
on calibration and ground-truthing of model results. More field observations are needed to verify the occurrence and improve  
405 the understanding of such events, also assessing their potential effect on subsequent water infiltration.

Our model results point to significant melt happening at negative temperatures, confirming earlier field observations: this  
would re-affirm the importance of using a full energy-balance model over a parametrized melt approach in cold conditions.  
Additional field investigations of the meteorological conditions at the onset of melt would be a valuable development.

Moreover, we found a novel trend of increasing surface melt amounts, currently on the edge of statistical significance.  
410 Further evolution of this tendency should be closely monitored, since in the near future it could affect the site suitability for  
retrieving climate records from ice cores. Estimations of local melt amounts may also contribute to the localization of future  
core drilling efforts: this provides motivation to attempt model deployment at other cold firn/ice sites and potentially on a larger  
scale.

For such an application, it would be beneficial to better constrain patterns and depths of meltwater percolation, by imple-  
415 menting a physical infiltration routine and acquiring vital calibration data. In addition to thermal tracking, recent developments  
in non-destructive analysis methods (e.g., Heilig et al., 2018; Katsushima et al., 2020) could advantageously serve this purpose.

*Code availability.* The EBFM code used in this study is available at <https://doi.org/10.5281/zenodo.4327090>. Due to their large volume,  
modeled grids are available upon request.



## Appendix A: Core *unifr-2019*

420 The 5.5 m firn core (Fig. A1) was recovered with a manually operated Kovacs Mark II corer. Firn density was measured in  
20 cm sections using a digital scale, while stratigraphy was visually inspected at a resolution of 0.5 cm. Mean core density is  
474 kg m<sup>-3</sup>, with a high variability and no clear densification trend towards depth. Relatively dense snow (up to 600 kg m<sup>-3</sup>)  
was encountered near the surface at around 0.5 m, with no ice layers concurrently observed. The first traces of refreezing were  
found at a depth of about 2 m. In total, 31 cm of refrozen layers could be identified, typically less than 2 cm thick and with  
425 variable ice content. At 4.5 m several ice-rich layers mixed with icy firn were found, over a contiguous thickness of 23 cm.

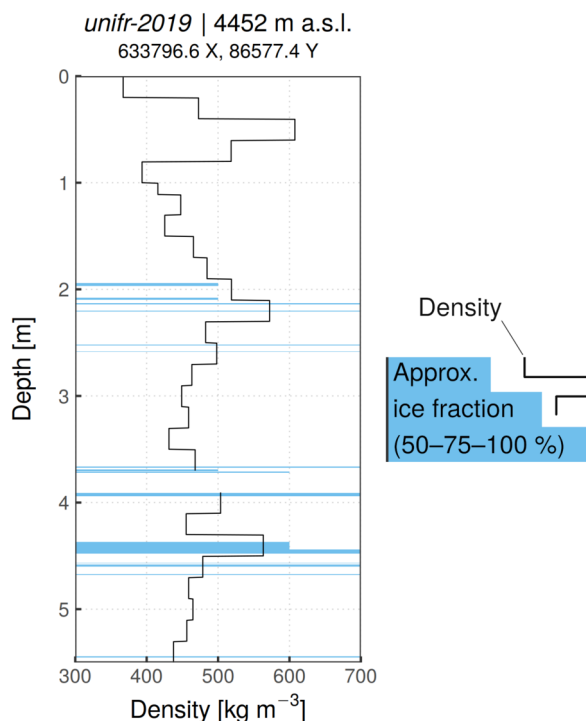


**Figure A1.** Density and stratigraphy of firn core *unifr-2019*. Values between 3.7 and 3.9 m are missing due to broken core during recovery. Drilling location is in metric CH1903/LV03 coordinates.

**Author contributions.** EM performed the analysis and wrote the paper. HM and EM drilled the firn core. MH provided unpublished data and previous works. All authors contributed to the discussion of the results. WvP supplied the EBFM model code and support to use it. MB provided the main meteorological data-set and extensive clarification on the CM AWS.





*Competing interests.* The authors declare that they have no conflict of interest.

430 *Acknowledgements.* We would like to thank Carlo Licciulli and Josef Lier (Heidelberg University) for supplying core, borehole and radar  
data. We would also like to thank ARPA Piemonte, the Italian Air Force Weather Service, MeteoSwiss, PERMOS and Visit Monte Rosa for  
providing access to the respective meteorological data. This work contains data/products of the Italian Air Force Weather Service. Swisstopo  
and Regione Piemonte provided the digital elevation models. Past firn temperature measurements were performed within the GLAMOS  
project, with funding by the Federal Office for the Environment FOEN, MeteoSwiss and the Swiss Academy of Sciences SCNAT. The legacy  
435 data collected in the Monte Rosa region was mainly organized and measured within the PhD thesis of Dr. Stephan Suter and was funded by  
the European Union Environment and Climate Programme under ENV4-CT97-0639 and the Swiss Government under BBW Nr. 97.0349-1,  
within the framework of the ALPCLIM EU project (Environmental and Climate records from high-elevation Alpine glaciers). MK, MH and  
HM acknowledge support by the Swiss National Science Foundation SNSF (grant 200021\_169453). This project has received funding from  
the European Research Council (ERC) under the European Union's Horizon 2020 research and innovation programme (project acronym  
440 CASSANDRA, grant agreement No. 818994).



## References

- Alean, J., Haeberli, W., and Schädler, B.: Snow accumulation, firn temperature and solar radiation in the area of the Colle Gnifetti core drilling site (Monte Rosa, Swiss Alps): distribution patterns and interrelationships, *Zeitschrift für Gletscherkunde und Glazialgeologie*, 19, 131–147, 1983.
- 445 ARPA Piemonte: Dati meteo orari, [https://www.arpa.piemonte.it/rischinaturali/accesso-ai-dati/Richieste-dati-formato-standard/richiesta-dati/Richiesta-automatica/Dati-meteo-orari.html?delta=1&\\$SCADENZA\\$=2](https://www.arpa.piemonte.it/rischinaturali/accesso-ai-dati/Richieste-dati-formato-standard/richiesta-dati/Richiesta-automatica/Dati-meteo-orari.html?delta=1&$SCADENZA$=2), last access December 2020, 2020.
- Auer, I., Böhm, R., and Schöner, W.: Chapter 3: Instrumental Climate, in: Final report of EU-rtd-project ALPCLIM, Zentralanstalt für Meteorologie und Geodynamik, Vienna, Austria, <http://www.zamg.ac.at/histalp/download/abstract/Auer-etal-2001c-F.pdf>, 2001.
- Barbante, C., Schwikowski, M., Döring, T., Gäggeler, H. W., Schotterer, U., Tobler, L., Van de Velde, K., Ferrari, C., Cozzi, G., Turetta,  
450 A., Rosman, K., Bolshov, M., Capodaglio, G., Cescon, P., and Boutron, C.: Historical Record of European Emissions of Heavy Metals to the Atmosphere Since the 1650s from Alpine Snow/Ice Cores Drilled near Monte Rosa, *Environmental Science & Technology*, 38, 4085–4090, <https://doi.org/10.1021/es049759r>, <https://pubs.acs.org/doi/10.1021/es049759r>, 2004.
- Beck, N., Wagenbach, D., and Münnich, K. O.: Laboratory experiments on the formation of solar radiation induced melt layers in dry snow, *Zeitschrift für Gletscherkunde und Glazialgeologie*, 24, 31–40, 1988.
- 455 Bohleber, P., Erhardt, T., Spaulding, N., Hoffmann, H., Fischer, H., and Mayewski, P.: Temperature and mineral dust variability recorded in two low-accumulation Alpine ice cores over the last millennium, *Climate of the Past*, 14, 21–37, <https://doi.org/10.5194/cp-14-21-2018>, <https://www.clim-past.net/14/21/2018/>, 2018.
- Bollmeyer, C., Keller, J. D., Ohlwein, C., Wahl, S., Crewell, S., Friederichs, P., Hense, A., Keune, J., Kneifel, S., Pscheidt, I., Redl, S., and Steinke, S.: Towards a high-resolution regional reanalysis for the European CORDEX domain: High-Resolution Regional Reanalysis  
460 for the European CORDEX Domain, *Quarterly Journal of the Royal Meteorological Society*, 141, 1–15, <https://doi.org/10.1002/qj.2486>, <http://doi.wiley.com/10.1002/qj.2486>, 2015.
- Bougamont, M., Bamber, J. L., and Greuell, W.: A surface mass balance model for the Greenland Ice Sheet, *Journal of Geophysical Research: Earth Surface*, 110, n/a–n/a, <https://doi.org/10.1029/2005JF000348>, <http://doi.wiley.com/10.1029/2005JF000348>, 2005.
- Buri, P.: Simulation of cold-firn-temperatures at an Alpine site using the model GEOTop, Master's thesis, University of Zürich, 2013.
- 465 Cannon, A. J., Sobie, S. R., and Murdock, T. Q.: Bias Correction of GCM Precipitation by Quantile Mapping: How Well Do Methods Preserve Changes in Quantiles and Extremes?, *Journal of Climate*, 28, 6938–6959, <https://doi.org/10.1175/JCLI-D-14-00754.1>, <http://journals.ametsoc.org/doi/10.1175/JCLI-D-14-00754.1>, 2015.
- Darms, G. A.: Firntemperaturen auf dem Colle Gnifetti: Zusammenstellung und Analyse bestehender und neuer Temperaturprofile, Master's thesis, University of Zürich, 2009.
- 470 Das, S. B. and Alley, R. B.: Characterization and formation of melt layers in polar snow: observations and experiments from West Antarctica, *Journal of Glaciology*, 51, 307–312, <https://doi.org/10.3189/172756505781829395>, [https://www.cambridge.org/core/product/identifier/S0022143000214937/type/journal\\_article](https://www.cambridge.org/core/product/identifier/S0022143000214937/type/journal_article), 2005.
- de Blasi, F., Gabrieli, J., Zhuravlev, A., Urbini, S., Burgay, F., Lodi, R., Dallo, F., Spolaor, A., Colucci, R. R., and Barbante, C.: Mt. Grand Combin ice core: correspondence among meteorological, morphological and geophysical evidence with ice core analysis, in: *Geophysical Research Abstracts*, vol. 21, Vienna, Austria, <https://meetingorganizer.copernicus.org/EGU2019/EGU2019-14393-2.pdf>, 2019.
- 475 Essery, R. and Etchevers, P.: Parameter sensitivity in simulations of snowmelt, *Journal of Geophysical Research*, 109, <https://doi.org/10.1029/2004JD005036>, <http://doi.wiley.com/10.1029/2004JD005036>, 2004.



- Feigenwinter, I., Kotlarski, S., Casanueva, A., Fischer, A., Schwierz, C., and Liniger, M.: Exploring quantile mapping as a tool to produce user-tailored climate scenarios for Switzerland, Tech. Rep. 270, MeteoSwiss, 2018.
- 480 Frank, C. W., Wahl, S., Keller, J. D., Pospichal, B., Hense, A., and Crewell, S.: Bias correction of a novel European reanalysis data set for solar energy applications, *Solar Energy*, 164, 12–24, <https://doi.org/10.1016/j.solener.2018.02.012>, <https://linkinghub.elsevier.com/retrieve/pii/S0038092X18301294>, 2018.
- Gabrieli, J., Cozzi, G., Vallelonga, P., Schwikowski, M., Sigl, M., Eickenberg, J., Wacker, L., Boutron, C., Gäggeler, H., Cescon, P., and Barbante, C.: Contamination of Alpine snow and ice at Colle Gnifetti, Swiss/Italian Alps, from nuclear weapons tests, *Atmospheric Environment*, 45, 587–593, <https://doi.org/10.1016/j.atmosenv.2010.10.039>, <https://linkinghub.elsevier.com/retrieve/pii/S1352231010009258>, 2011.
- 485 Gilbert, A., Vincent, C., Six, D., Wagnon, P., Piard, L., and Ginot, P.: Modeling near-surface firn temperature in a cold accumulation zone (Col du Dôme, French Alps): from a physical to a semi-parameterized approach, *The Cryosphere*, 8, 689–703, <https://doi.org/10.5194/tc-8-689-2014>, <https://www.the-cryosphere.net/8/689/2014/>, 2014.
- 490 GLAMOS: The Swiss Glaciers 2013/14 and 2014/15 Glaciological Report No. 135/136, Tech. rep., Cryospheric Commission (EKK) of the Swiss Academy of Sciences (SCNAT); Laboratory of Hydraulics, Hydrology and Glaciology (VAW), Swiss Federal Institute of Technology Zurich (ETH Zurich), [https://doi.org/10.18752/GLREP\\_135-136](https://doi.org/10.18752/GLREP_135-136), 2017.
- Greuell, W. and Konzelmann, T.: Numerical modelling of the energy balance and the englacial temperature of the Greenland Ice Sheet. Calculations for the ETH-Camp location (West Greenland, 1155 m a.s.l.), *Global and Planetary Change*, 9, 91–114, [https://doi.org/10.1016/0921-8181\(94\)90010-8](https://doi.org/10.1016/0921-8181(94)90010-8), <https://linkinghub.elsevier.com/retrieve/pii/0921818194900108>, 1994.
- 495 Greuell, W., Knap, W. H., and Smeets, P. C.: Elevational changes in meteorological variables along a midlatitude glacier during summer, *Journal of Geophysical Research: Atmospheres*, 102, 25 941–25 954, <https://doi.org/10.1029/97JD02083>, <http://doi.wiley.com/10.1029/97JD02083>, 1997.
- Gruber, S., King, L., Kohl, T., Herz, T., Haeberli, W., and Hoelzle, M.: Interpretation of geothermal profiles perturbed by topography: the alpine permafrost boreholes at Stockhorn Plateau, Switzerland, *Permafrost and Periglacial Processes*, 15, 349–357, <https://doi.org/10.1002/ppp.503>, <http://doi.wiley.com/10.1002/ppp.503>, 2004.
- 500 Haeberli, W. and Beniston, M.: Climate Change and Its Impacts on Glaciers and Permafrost in the Alps, *Ambio*, 27, 258–265, <http://www.jstor.org/stable/4314732>, 1998.
- Haeberli, W. and Funk, M.: Borehole temperatures at the Colle Gnifetti core-drilling site (Monte Rosa, Swiss Alps), *Journal of Glaciology*, 37, 37–46, <https://doi.org/10.3189/S0022143000042775>, [https://www.cambridge.org/core/product/identifier/S0022143000042775/type/journal\\_article](https://www.cambridge.org/core/product/identifier/S0022143000042775/type/journal_article), 1991.
- 505 Harper, J., Humphrey, N., Pfeffer, W. T., Brown, J., and Fettweis, X.: Greenland ice-sheet contribution to sea-level rise buffered by meltwater storage in firn, *Nature*, 491, 240–243, <https://doi.org/10.1038/nature11566>, <http://www.nature.com/articles/nature11566>, 2012.
- Heilig, A., Eisen, O., MacFerrin, M., Tedesco, M., and Fettweis, X.: Seasonal monitoring of melt and accumulation within the deep percolation zone of the Greenland Ice Sheet and comparison with simulations of regional climate modeling, *The Cryosphere*, 12, 1851–1866, <https://doi.org/10.5194/tc-12-1851-2018>, <https://www.the-cryosphere.net/12/1851/2018/>, 2018.
- 510 Hoelzle, M., Darms, G., Lüthi, M. P., and Suter, S.: Evidence of accelerated englacial warming in the Monte Rosa area, Switzerland/Italy, *The Cryosphere*, 5, 231–243, <https://doi.org/10.5194/tc-5-231-2011>, <http://www.the-cryosphere.net/5/231/2011/>, 2011.
- Illangasekare, T. H., Walter, R. J., Meier, M. F., and Pfeffer, W. T.: Modeling of meltwater infiltration in subfreezing snow, *Water Resources Research*, 26, 1001–1012, <https://doi.org/10.1029/WR026i005p01001>, <http://doi.wiley.com/10.1029/WR026i005p01001>, 1990.
- 515



- Jenk, T. M., Szidat, S., Bolius, D., Sigl, M., Gäggeler, H. W., Wacker, L., Ruff, M., Barbante, C., Boutron, C. F., and Schwikowski, M.: A novel radiocarbon dating technique applied to an ice core from the Alps indicating late Pleistocene ages, *Journal of Geophysical Research*, 114, <https://doi.org/10.1029/2009JD011860>, <http://doi.wiley.com/10.1029/2009JD011860>, 2009.
- 520 Katsushima, T., Adachi, S., Yamaguchi, S., Ozeki, T., and Kumakura, T.: Nondestructive three-dimensional observations of flow finger and lateral flow development in dry snow using magnetic resonance imaging, *Cold Regions Science and Technology*, 170, 102956, <https://doi.org/10.1016/j.coldregions.2019.102956>, <https://linkinghub.elsevier.com/retrieve/pii/S0165232X19301119>, 2020.
- Klok, E. and Oerlemans, J.: Model study of the spatial distribution of the energy and mass balance of Morteratschgletscher, Switzerland, *Journal of Glaciology*, 48, 505–518, <https://doi.org/10.3189/172756502781831133>, [https://www.cambridge.org/core/product/identifier/S0022143000209623/type/journal\\_article](https://www.cambridge.org/core/product/identifier/S0022143000209623/type/journal_article), 2002.
- 525 Koerner, R.: The Mass Balance of the Devon Island Ice Cap, Northwest Territories, Canada, 1961–66, *Journal of Glaciology*, 9, 325–336, <https://doi.org/10.3189/S0022143000022863>, [https://www.cambridge.org/core/product/identifier/S0022143000022863/type/journal\\_article](https://www.cambridge.org/core/product/identifier/S0022143000022863/type/journal_article), 1970.
- Konrad, H., Bohleber, P., Wagenbach, D., Vincent, C., and Eisen, O.: Determining the age distribution of Colle Gnifetti, Monte Rosa, Swiss Alps, by combining ice cores, ground-penetrating radar and a simple flow model, *Journal of Glaciology*, 59, 179–189, <https://doi.org/10.3189/2013JoG12J072>, [https://www.cambridge.org/core/product/identifier/S0022143000203511/type/journal\\_article](https://www.cambridge.org/core/product/identifier/S0022143000203511/type/journal_article), 2013.
- 530 Konzelmann, T., Vandewal, R., Greuell, W., Bintanja, R., Henneken, E., and Abeouchi, A.: Parameterization of global and longwave incoming radiation for the Greenland Ice Sheet, *Global and Planetary Change*, 9, 143–164, [https://doi.org/10.1016/0921-8181\(94\)90013-2](https://doi.org/10.1016/0921-8181(94)90013-2), <https://linkinghub.elsevier.com/retrieve/pii/0921818194900132>, 1994.
- 535 Kuhn, M.: Micro-Meteorological Conditions for Snow Melt, *Journal of Glaciology*, 33, 24–26, <https://doi.org/10.3189/S002214300000530X>, [https://www.cambridge.org/core/product/identifier/S002214300000530X/type/journal\\_article](https://www.cambridge.org/core/product/identifier/S002214300000530X/type/journal_article), 1987.
- Licciulli, C.: Full Stokes ice-flow modeling of the high-Alpine glacier saddle Colle Gnifetti, Monte Rosa: Flow field characterization for an improved interpretation of the ice-core records, Ph.D. thesis, University of Heidelberg, 2018.
- Lier, J.: Estimating the amount of latent heat released by refreezing surface melt water for the high-Alpine glacier saddle Colle Gnifetti, Swiss/Italian Alps, Master's thesis, University of Heidelberg, 2018.
- 540 Lüthi, M. P.: Rheology of cold firn and dynamics of a polythermal ice stream: Studies on Colle Gnifetti and Jakobshavn Isbræ, Ph.D. thesis, ETH Zürich, <https://doi.org/10.3929/ethz-a-003884174>, <http://hdl.handle.net/20.500.11850/144542>, 2000.
- Lüthi, M. P. and Funk, M.: Modelling heat flow in a cold, high-altitude glacier: interpretation of measurements from Colle Gnifetti, Swiss Alps, *Journal of Glaciology*, 47, 314–324, <https://doi.org/10.3189/172756501781832223>, [https://www.cambridge.org/core/product/identifier/S0022143000211027/type/journal\\_article](https://www.cambridge.org/core/product/identifier/S0022143000211027/type/journal_article), 2001.
- 545 Marchenko, S., van Pelt, W. J. J., Claremar, B., Pohjola, V., Pettersson, R., Machguth, H., and Reijmer, C.: Parameterizing Deep Water Percolation Improves Subsurface Temperature Simulations by a Multilayer Firn Model, *Frontiers in Earth Science*, 5, <https://doi.org/10.3389/feart.2017.00016>, <http://journal.frontiersin.org/article/10.3389/feart.2017.00016/full>, 2017.
- Martorina, S., Olivero, A., Loglisci, N., and Pelosini, R.: La stazione meteo più alta d'Europa, Neve e Valanghe, 49, <https://issuu.com/aineva7/docs/nv49>, 2003.
- 550 Mattea, E.: Measuring and modelling changes in the firn at Colle Gnifetti, 4400 m a.s.l., Swiss Alps, Master's thesis, University of Fribourg, [https://bigweb.unifr.ch/Science/Geosciences/GeographyTechnical/Secretary/Pub/Publications/Geography/SelectedBachelorMasterThesis/2020/Mattea\\_E.\\_\(2020\)\\_M\\_Measuring\\_modelling\\_changes\\_Colle\\_Gnifetti.pdf](https://bigweb.unifr.ch/Science/Geosciences/GeographyTechnical/Secretary/Pub/Publications/Geography/SelectedBachelorMasterThesis/2020/Mattea_E._(2020)_M_Measuring_modelling_changes_Colle_Gnifetti.pdf), 2020.



- 555 MeteoAM: Servizio Meteorologico dell'Aeronautica Militare - Disponibilità dei dati, [http://www.meteoam.it/dati\\_in\\_tempo\\_reale](http://www.meteoam.it/dati_in_tempo_reale), last access December 2020, 2020.
- MeteoSwiss: Data portal for experts, <https://www.meteoswiss.admin.ch/home/services-and-publications/beratung-und-service/datenportal-fuer-experten.html>, last access December 2020, 2020.
- 560 More, A. F., Spaulding, N. E., Bohleber, P., Handley, M. J., Hoffmann, H., Korotkikh, E. V., Kurbatov, A. V., Loveluck, C. P., Sneed, S. B., McCormick, M., and Mayewski, P. A.: Next-generation ice core technology reveals true minimum natural levels of lead (Pb) in the atmosphere: Insights from the Black Death, *GeoHealth*, 1, 211–219, <https://doi.org/10.1002/2017GH000064>, <https://onlinelibrary.wiley.com/doi/abs/10.1002/2017GH000064>, 2017.
- New, M., Hulme, M., and Jones, P.: Representing Twentieth-Century Space–Time Climate Variability. Part II: Development of 1901–96 Monthly Grids of Terrestrial Surface Climate, *Journal of Climate*, 13, 2217–2238, [https://doi.org/10.1175/1520-0442\(2000\)013<2217:RTCSTC>2.0.CO;2](https://doi.org/10.1175/1520-0442(2000)013<2217:RTCSTC>2.0.CO;2), <http://journals.ametsoc.org/doi/abs/10.1175/1520-0442%282000%29013%3C2217%3ARTCSTC%3E2.0.CO%3B2>, 2000.
- 565 Oerlemans, J. and Grisogono, B.: Glacier winds and parameterisation of the related surface heat fluxes, *Tellus A*, 54, 440–452, <https://doi.org/10.1034/j.1600-0870.2002.201398.x>, <http://tellusa.net/index.php/tellusa/article/view/12164>, 2002.
- Oerlemans, J. and Knap, W. H.: A 1 year record of global radiation and albedo in the ablation zone of Morteratschgletscher, Switzerland, *Journal of Glaciology*, 44, 231–238, <https://doi.org/10.1017/S0022143000002574>, [https://www.cambridge.org/core/product/identifier/S0022143000002574/type/journal\\_article](https://www.cambridge.org/core/product/identifier/S0022143000002574/type/journal_article), 1998.
- 570 Quéno, L., Fierz, C., van Herwijnen, A., Longridge, D., and Wever, N.: Deep ice layer formation in an alpine snowpack: monitoring and modeling, *The Cryosphere*, 14, 3449–3464, <https://doi.org/10.5194/tc-14-3449-2020>, <https://tc.copernicus.org/articles/14/3449/2020/>, 2020.
- Regione Piemonte: RIPRESA AEREA ICE 2009-2011 – DTM 5, <http://www.geoportale.piemonte.it/geonetworkkrp/srv/ita/metadata.show?id=2552&currTab=rndt>, last access November 2020, 2011.
- 575 Reijmer, C. H., van Meijgaard, E., and van den Broeke, M. R.: Evaluation of temperature and wind over Antarctica in a Regional Atmospheric Climate Model using 1 year of automatic weather station data and upper air observations, *Journal of Geophysical Research*, 110, <https://doi.org/10.1029/2004JD005234>, <http://doi.wiley.com/10.1029/2004JD005234>, 2005.
- Rossi, G., Johnston, P., and Maggi, V.: ALPCLIM project: Reconstruction of the monthly values of solar radiation incident over the Lys Glacier surface (Monte Rosa-Western Italian Alps), in: 26th Intl. Conference on Alpine Meteorology, ICAM, Innsbruck, 2000a.
- 580 Rossi, G., Johnston, P., and Maggi, V.: Project ALPCLIM: Résultats de l'observation météorologique dans le site de Colle du Lys (4250 mètres), in: Réunion Annuelle Société Hydrotechnique de France, Section Glaciologie, Société Hydrotechnique de France, Grenoble, 2000b.
- Schwikowski, M.: Reconstruction of European Air Pollution from Alpine Ice Cores, in: *Earth Paleoenvironments: Records Preserved in Mid- and Low-Latitude Glaciers*, edited by DeWayne Cecil, L., Green, J. R., and Thompson, L. G., vol. 9, pp. 95–119, Kluwer Academic Publishers, Dordrecht, [https://doi.org/10.1007/1-4020-2146-1\\_6](https://doi.org/10.1007/1-4020-2146-1_6), [http://link.springer.com/10.1007/1-4020-2146-1\\_6](http://link.springer.com/10.1007/1-4020-2146-1_6), series Title: *Developments in Paleoenvironmental Research*, 2004.
- 585 Shumskii, P. A.: *Principles of Structural Glaciology: The Petrography of Fresh-water Ice as a Method of Glaciological Investigation*, Dover Publications Inc., New York, 1964.
- Suter, S.: Cold firn and ice in the Monte Rosa and Mont Blanc areas: spatial occurrence, surface energy balance and climatic evidence, Ph.D. thesis, ETH Zürich, <https://doi.org/10.3929/ethz-a-004288434>, <http://hdl.handle.net/20.500.11850/145885>, 2002.
- 590



- Suter, S. and Hoelzle, M.: Cold firn in the Mont Blanc and Monte Rosa areas, European Alps: spatial distribution and statistical models, *Annals of Glaciology*, 35, 9–18, <https://doi.org/10.3189/172756402781817059>, [https://www.cambridge.org/core/product/identifier/S0260305500257200/type/journal\\_article](https://www.cambridge.org/core/product/identifier/S0260305500257200/type/journal_article), 2002.
- 595 Suter, S., Laternser, M., Haeberli, W., Frauenfelder, R., and Hoelzle, M.: Cold firn and ice of high-altitude glaciers in the Alps: measurements and distribution modelling, *Journal of Glaciology*, 47, 85–96, <https://doi.org/10.3189/172756501781832566>, [https://www.cambridge.org/core/product/identifier/S0022143000212264/type/journal\\_article](https://www.cambridge.org/core/product/identifier/S0022143000212264/type/journal_article), 2001.
- Suter, S., Hoelzle, M., and Ohmura, A.: Energy balance at a cold Alpine firn saddle, Seserjoch, Monte Rosa, *International Journal of Climatology*, 24, 1423–1442, <https://doi.org/10.1002/joc.1079>, <http://doi.wiley.com/10.1002/joc.1079>, 2004.
- 600 van Pelt, W., Pohjola, V., Pettersson, R., Marchenko, S., Kohler, J., Luks, B., Hagen, J. O., Schuler, T. V., Dunse, T., Noël, B., and Reijmer, C.: A long-term dataset of climatic mass balance, snow conditions, and runoff in Svalbard (1957–2018), *The Cryosphere*, 13, 2259–2280, <https://doi.org/10.5194/tc-13-2259-2019>, <https://www.the-cryosphere.net/13/2259/2019/>, 2019.
- van Pelt, W. J. and Kohler, J.: Modelling the long-term mass balance and firn evolution of glaciers around Kongsfjorden, Svalbard, *Journal of Glaciology*, 61, 731–744, <https://doi.org/10.3189/2015JoG14J223>, [https://www.cambridge.org/core/product/identifier/S0022143000202542/type/journal\\_article](https://www.cambridge.org/core/product/identifier/S0022143000202542/type/journal_article), 2015.
- 605 van Pelt, W. J. J., Oerlemans, J., Reijmer, C. H., Pohjola, V. A., Pettersson, R., and van Angelen, J. H.: Simulating melt, runoff and refreezing on Nordenskiöldbreen, Svalbard, using a coupled snow and energy balance model, *The Cryosphere*, 6, 641–659, <https://doi.org/10.5194/tc-6-641-2012>, <https://www.the-cryosphere.net/6/641/2012/>, 2012.
- Vandecrux, B., Mottram, R., Langen, P. L., Fausto, R. S., Olesen, M., Stevens, C. M., Verjans, V., Leeson, A., Ligtenberg, S., Kuipers Munneke, P., Marchenko, S., van Pelt, W., Meyer, C. R., Simonsen, S. B., Heilig, A., Samimi, S., Marshall, S., Machguth, H., MacFerrin, M., Niwano, M., Miller, O., Voss, C. I., and Box, J. E.: The firn meltwater Retention Model Intercomparison Project (RetMIP): evaluation of nine firn models at four weather station sites on the Greenland ice sheet, *The Cryosphere*, 14, 3785–3810, <https://doi.org/10.5194/tc-14-3785-2020>, <https://tc.copernicus.org/articles/14/3785/2020/>, 2020.
- Visit Monte Rosa: Stazioni meteo Monte Rosa Val d’Aosta e Piemonte, <https://www.visitmonterosa.com/stazioni-meteo/>, last access December 2020, 2020.
- 615 Wagenbach, D., Bohleber, P., and Preunkert, S.: Cold, alpine ice bodies revisited: what may we learn from their impurity and isotope content?, *Geografiska Annaler: Series A, Physical Geography*, 94, 245–263, <https://doi.org/10.1111/j.1468-0459.2012.00461.x>, <https://www.tandfonline.com/doi/full/10.1111/j.1468-0459.2012.00461.x>, 2012.
- Wahl, S., Bollmeyer, C., Crewell, S., Figura, C., Friederichs, P., Hense, A., Keller, J. D., and Ohlwein, C.: A novel convective-scale regional reanalysis COSMO-REA2: Improving the representation of precipitation, *Meteorologische Zeitschrift*, 26, 345–361, <https://doi.org/10.1127/metz/2017/0824>, [http://www.schweizerbart.de/papers/metz/detail/26/87333/A\\_novel\\_convective\\_scale\\_regional\\_reanalysis\\_COSMO?af=crossref](http://www.schweizerbart.de/papers/metz/detail/26/87333/A_novel_convective_scale_regional_reanalysis_COSMO?af=crossref), 2017.
- 620